The International Journal of Advanced Manufacturing Technology (2025) 139:4959–4969
https://doi.org/10.1007/s00170-025-16062-0

ORIGINAL ARTICLE

Diffusion coefficients of graphite foil carbon in Mo during spark plasma sintering process

William Baya Mwaro[1,3] · **Mahlatse R. Mphahlele**[2] · **Mark Walker**[1]

Received: 15 April 2025 / Accepted: 1 July 2025 / Published online: 1 August 2025

Abstract
This study investigated the influence of electric current on carbon diffusivity in molybdenum (Mo) during spark plasma sintering (SPS). The samples comprised 0.2-mm-thick graphite foils, 3-mm Mo discs annealed at 1000 °C for 1–8 h, and a Ti-Mo alloy annealed at 1200 °C for 4 h. Elemental concentration profiles were analyzed using electron probe microanalysis (EPMA), while microstructure evolution was examined via scanning electron microscopy (SEM), electron backscatter diffraction (EBSD), and transmission electron microscopy (TEM) in various modes. Diffusion coefficients were determined using the Den Broeder method and compared with literature values to assess possible enhancement. Contrary to expectations, the results indicated no enhancement of diffusion coefficients under electric current; instead, they decreased with increasing carbon concentration. This reduction was attributed to the formation of a molybdenum carbide layer, which hinders further carbon diffusion into the Mo matrix. The study also observed that diffusion of carbon into the sample occurs predominantly via solid-state diffusion at the graphite-metal interface, rather than vapor-phase transport.

Keywords Spark plasma sintering · Graphite foil · Carbon contamination · Electric current diffusion enhancement

1 Introduction

Spark plasma sintering (SPS), a prominent field–assisted sintering technique (FAST), utilizes electric current to enhance densification through Joule heating and other electro-kinetic effects. Beyond thermal activation, the applied current has been shown to exert non-thermal influences that accelerate diffusion-related processes, such as vacancy formation [1], intermetallic phase growth [2], and defect mobility [3]—thereby significantly altering sintering kinetics and microstructure evolution—influencing sintering kinetics and microstructure evolution [4]. However, a critical yet often overlooked aspect of SPS is the unintended diffusion of carbon atoms from the tooling (e.g., graphite dies, punches, and foils) into the sintered material, a phenomenon commonly referred to as carbon contamination [5, 6]. Among the SPS tooling components, graphite foils play a key role in carbon contamination. These foils serve as protective and conductive layers, ensuring efficient heat transfer and uniform current distribution. However, direct contact between the graphite foil and the sample facilitates carbon diffusion into the material – a phenomenon known as carbon contamination. Carbon contamination is known to adversely affect the structural and mechanical properties of refractory materials [5, 7]. For instance, during processing of Mo using SPS, carbon contamination has been shown to induce embrittlement and a marked reduction in ductility. This degradation arises from the precipitation of brittle molybdenum carbides (Mo_2C, MoC) along grain boundaries upon cooling. These carbides serve as preferential sites for crack initiation and propagation, significantly diminishing fracture toughness and promoting brittle failure at low stress [8, 9].

Beyond mechanical degradation, molybdenum carbides exhibit inferior thermal and electrical conductivity compared to pure Mo, diminishing the material's efficacy in electrical and thermal management applications, such as electrodes and heat sinks. Furthermore, differential thermal expansion between carbide phases and the Mo matrix induces localized

✉ William Baya Mwaro
williambayam@gmail.com

[1] Department of Mechanical Engineering, Durban University of Technology, Durban 4001, South Africa

[2] Department of Mechanical & Mechatronic Engineering, Cape Peninsula University of Technology, Cape Town (Belville) 7535, South Africa

[3] School of Mines and Engineering, Taita Taveta University, P.O Box 635 - (80300), Voi, Kenya

stresses during thermal cycling, exacerbating microcrack formation and reducing thermal shock resistance [10]. Additionally, carbon segregation influences grain boundary mobility, leading to heterogeneous grain growth and the development of a bimodal grain structure, which undermines mechanical uniformity [11]. These findings underscore the critical need for stringent control of carbon content in refractory systems to preserve their structural stability, mechanical performance, and functional utility in high-temperature and load-bearing applications.

While prior research has extensively documented carbon contamination from graphite foils, few studies have investigated the underlying diffusion kinetics. Notably, Morita et al. [12, 13] examined carbon diffusion in metallic samples but focused primarily on general diffusion behavior without considering the influence of electric current—a defining feature of SPS. Their conclusion that carbon migration occurs mainly via grain boundary evaporation leaves a gap in understanding solid-state diffusion, particularly under electrically assisted sintering conditions where direct graphite-sample contact plays a critical role. In this study therefore, the existing gap was addressed by systematically investigating whether electric current during SPS process enhances carbon diffusion from graphite foils into metallic samples. Additionally, by modifying the standard SPS tooling configuration, the study also investigated the solid-state diffusion of carbon atoms resulting from direct contact between graphite foil and a metallic sample.

1.1 Theoretical considerations

Atomic diffusion involves the thermal excitation of atoms leading to stochastic jumps across lattice sites. Thus, temperature serves as the primary governing parameter in diffusion kinetics and related analyses. However, in metallic systems, the passage of an electric current introduces an additional, non-thermal driving force (electromigration) which alters atomic mobility through momentum transfer between conducting electrons [14]. Furthermore, applied mechanical pressure modifies the activation volume for diffusion, influencing atomic migration pathways [15]. Thus, while Fick's second law classically describes diffusion in terms of concentration gradients, the spark plasma sintering (SPS) process—which simultaneously employs pulsed electric currents and uniaxial pressure—introduces a complex interplay of thermal, electrical, and mechanical fields. This multi-physics coupling complicates the direct application of conventional diffusion models. To adapt Fickian analysis to the SPS environment therefore, various assumptions were employed. Firstly, for a given annealing temperature, diffusion was assumed to primarily be governed by chemical potential gradients, with concentration-driven flux remaining the principal mechanism. Secondly, electromigration, microstructure evolution, and other atomic-level effects were treated as perturbations that either enhanced or suppressed the effective diffusion coefficient. Thirdly, diffusivity was assumed to be spatially uniform and directionally invariant, neglecting localized anisotropies arising from grain boundaries or stress gradients. Lastly, the diffusivity of a non-metal was assumed to be substantially higher than that of the host metal hence the reaction diffusion in the Mo-C system was regarded as the diffusion of carbon in a metal grid of Mo.

Consequently, the diffusion process was described by the 2nd Fick's law of diffusion as [16]:

$$\frac{\partial \mathrm{C}}{\partial \mathrm{t}} = \frac{\partial}{\partial \mathrm{x}}\left(\mathrm{D}\frac{\partial \mathrm{C}}{\partial \mathrm{x}}\right) \tag{1}$$

where C is the concentration, t is diffusion time, and x is the diffusion distance. When the concentration of the in-diffusing species changes with distance from the initial contact surface, the diffusion coefficient also becomes concentration-dependent. In establishing the concentration-dependent diffusion coefficient, D(C), Eq. 1 may be transformed using the Boltzmann-Matano variable, $y = x/2\sqrt{t}$ [17] into its ordinary differential form as:

$$-2\mathrm{y}\frac{\mathrm{dC}}{\mathrm{dy}} = \frac{\mathrm{d}}{\mathrm{dy}}\left(\mathrm{D(C)}\frac{\mathrm{dC}}{\mathrm{dx}}\right) \tag{2}$$

From Eq. 2, D(C) may be evaluated using the Boltzmann-Matano method [17] which is generally a method of derivatives in which D(C) is obtained through integration by parts of the time and space form of Eq. 2 as:

$$\mathrm{D(C^*)} = \frac{1}{2\mathrm{t}(\mathrm{dC/dx})_{\mathrm{C^*}}}\left(\mathrm{x^* - x_M}\right)\mathrm{C^*}\int_{\mathrm{x^*}}^{-\infty}\mathrm{Cdx} \tag{3}$$

where x_{M} is the position of the Matano plane which may be established from the flux conservation condition given in Eq. 4[].

$$x_M = \int_0^1 \mathrm{C}dx = \int_{\infty}^{0}(1-\mathrm{C})\mathrm{d}x + \int_0^{+\infty}\mathrm{C}(x)\mathrm{d}x \tag{4}$$

The Boltzmann-Matano method was modified by Sauer-Freise and later by Den-Broeder [18] by combining Eqs. (4) and (3) and introducing the concentration normalization variable, Y. For constant volume, the Sauer-Freise/Den Broeder equation for D(C) is given as:

$$\mathrm{D(C^*)} = \frac{1}{2\mathrm{t}}\left(\frac{\mathrm{dx}}{\mathrm{dC}}\right)\left[(1-\mathrm{Y})\int_{-\infty}^{x^*}(\mathrm{C^* - C^-})\mathrm{dx} + \mathrm{Y}\int_{x^*}^{+\infty}\left(\mathrm{C^+ - C^*}\right)\mathrm{dx}\right] \tag{5}$$

where C^* is the concentration at the position x^*, C^- is the minimum concentration, C^+ is the maximum concentration of the diffusing species, and x is the distance across the diffusion region. The normalized composition variable, Y is given by:

$$Y = \frac{C(x) - C^-}{C^+ - C^-} \tag{6}$$

2 Materials and methods

2.1 Sample design, processing, and annealing

Traditionally, spark plasma sintering is designed for the production of parts from powdered materials. However, diffusion in powder particles can be complex and multidirectional. For the evaluation of diffusion coefficients using standard expressions, a continuous unidirectional diffusion profile is preferable. Thus, in this study, bulk samples were used in place of powdered samples. The study comprised of two sets of annealing experiments conducted using a spark plasma sintering (SPS) system (HDP 25, FCT Systeme GmbH, Germany) at the Institute of Materials Science, TU Bergakademie Freiberg (TUBAF), Germany. The first set involved the annealing of individual 3-mm-thick molybdenum (Mo) discs, while the second set examined diffusion of graphite foil carbon in a binary Ti-Mo alloy. The starting materials consisted of high-purity Mo (99.7%) and Ti (99.8%) rods (20 mm diameter supplied by Alfar Aesar). From these, four 3-mm-thick Mo discs, two 5-mm-thick Mo discs, and one 5-mm-thick Ti disc were precision-cut and metallographically polished to a 1-µm surface finish. Graphite foils (0.2 mm thick, SIGRAFLEX® by SGL Group) were cut into 20-mm-diameter discs, with two foils used per experiment to separate the samples from the SPS punches, following standard SPS protocols. Thus, for the purpose of this study, the final configuration of the Mo disc samples consisted of the graphite foil–Mo–graphite foil (C-M-C). For the Mo disc experiments, each C-Mo-C sample was annealed separately at 1000 °C for durations of 1, 2, 4, and 8 h. In the Ti-Mo alloy experiment, the 5-mm discs were arranged in a Mo-Ti-Mo stack configuration. In the presence of the graphite foils, the final configuration of the Ti-Mo alloy sample was graphite foil-Mo-Ti-Mo-graphite foil (C-Mo-Ti-Mo-C). Annealing of the C-Mo-Ti-Mo-C sample was carried out at 1200 °C for 4 h. In both cases, the graphite die interior was lined with corundum (Al_2O_3) foil to prevent carbon diffusion from the die walls and to ensure that all the current was flowing through the sample. A uniaxial pressure of 15 MPa was applied hydraulically throughout the annealing process to maintain optimal contact between the sample, the tooling, and electrodes. To prevent directional-dependent diffusion effects emerging from high current density electromigration [19], the current densities in this case were set at low values of 188 A cm^{-2} for the C-Mo-C samples and 177 A cm^{-2} for the C-Mo-Ti-Mo-C stack. Heating proceeded at 160 K min^{-1}, followed by rapid cooling (~ 200 K min^{-1}) via water circulation through the electrodes. Temperature was monitored in real-time using an optical pyrometer aligned with a borehole in the upper punch.

2.2 Analytical methods

Analysis of microstructure evolution was conducted on the materials in “as supplied form” (Ti &Mo) and after annealing. Before annealing, sample materials were analyzed using the scanning electron microscope (SEM) in energy dispersion spectroscopy (EDX) mode and using the electron back scatter diffraction (EBSD). Annealed samples were analyzed in secondary electrons (SE) and back scattered electron (BSE) modes, i.e., SEM (SE and BSE). The device used for SEM analysis was the Zeiss FEG-SEM LEO 1530 GEMINI equipped with an EBSD detector. To optimize resolution while minimizing shadowing effects, moderately low working distances (WD) were used: 8–9 mm for secondary electron (SE) and backscattered electron (BSE) imaging, and 16 mm for electron backscatter diffraction (EBSD). These values align with established standards for high-resolution SEM [20]. In SE and BSE, the range of 8–9 mm was necessary to accommodate variations in sample surface quality. EBSD patterns acquired were processed further using Channel 5 HKL software from Oxford Instruments. For nanoscale microstructural features beyond EBSD resolution, transmission electron microscopy was conducted using a JEOL JEM 2010 FEF instrument. TEM specimens were prepared via focused ion beam (FIB) milling and analyzed in both scanning TEM (STEM) and high-resolution TEM (HRTEM) modes. Diffraction pattern analysis involved measuring interplanar spacings from selected-area electron diffraction (SAED) patterns and comparing these with reference data from the ICSD database. Elemental composition analysis was performed via electron probe microanalysis (EPMA) using a JEOL JXA8900RL system, with concentration measurements taken at 1-µm intervals to map the spatial distribution of carbon, molybdenum, and titanium. The diffusion coefficients were evaluated using Eq. 5 which was implemented in a routine written in MATLAB. MATLAB is a commercial programming environment developed by Math Works Inc., MA, USA.

3 Results and discussion

3.1 Microstructure of the starting materials

Figure 1a and b are EBSD micrographs of the starting Mo and Ti respectively. From the images, pure Mo consisted of small grains that were randomly oriented while pure Ti consisted of large grains which were oriented between 30 and 60° and between 85 and 94° with respect to the {0001} plane. The average grain size of Mo was $7 \pm 0.5\ \mu m$ and that of Ti was $50 \pm 0.5\ \mu m$ while the grain boundary density per unit length was higher in Mo compared to Ti (Fig. 1 a and b). The elemental EDX spectrum of both Mo and Ti (inset Fig. 1) confirmed that both materials did not contain either dissolved carbon or any other foreign elements.

3.2 Characterization of diffused carbon in Mo

The EDX and XRD measurements on the annealed samples revealed the presence of diffused carbon in Mo in both the 3-mm Mo discs and in the Ti-Mo alloy samples (Fig. 2). The two peaks in SEM–EDX spectrum (Fig. 2a) were indexed as Mo and carbon while the XRD pattern (Fig. 2b) showed peaks distribution at 2θ (°) angles of 34, 37, 39, 52, and 61. This peak distribution matched

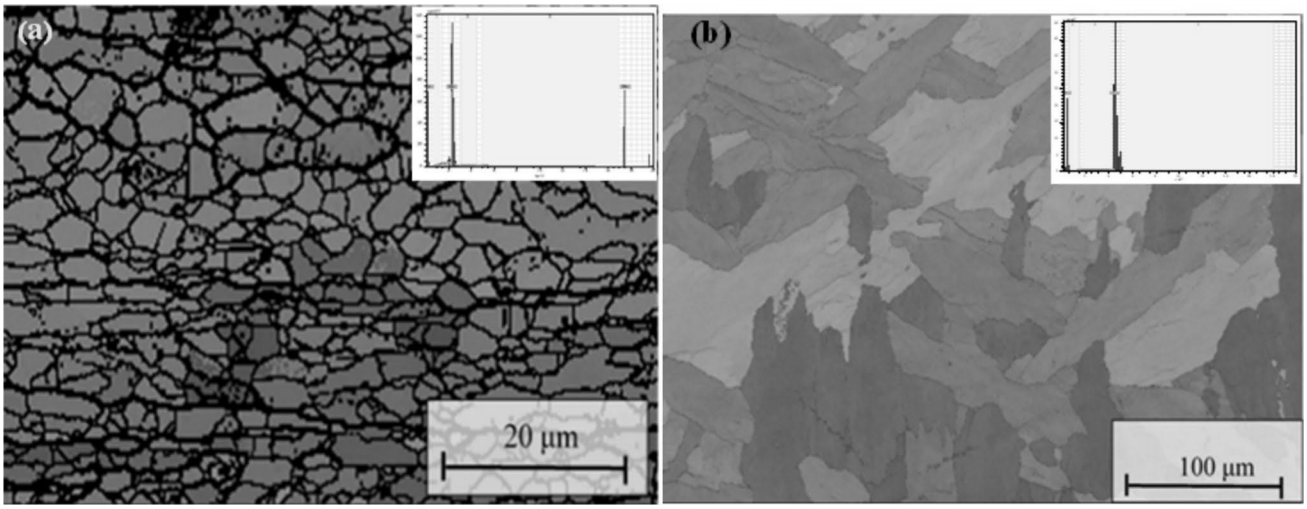

Fig. 1 Microstructure of the starting materials (**a**) Mo and (**b**) Ti

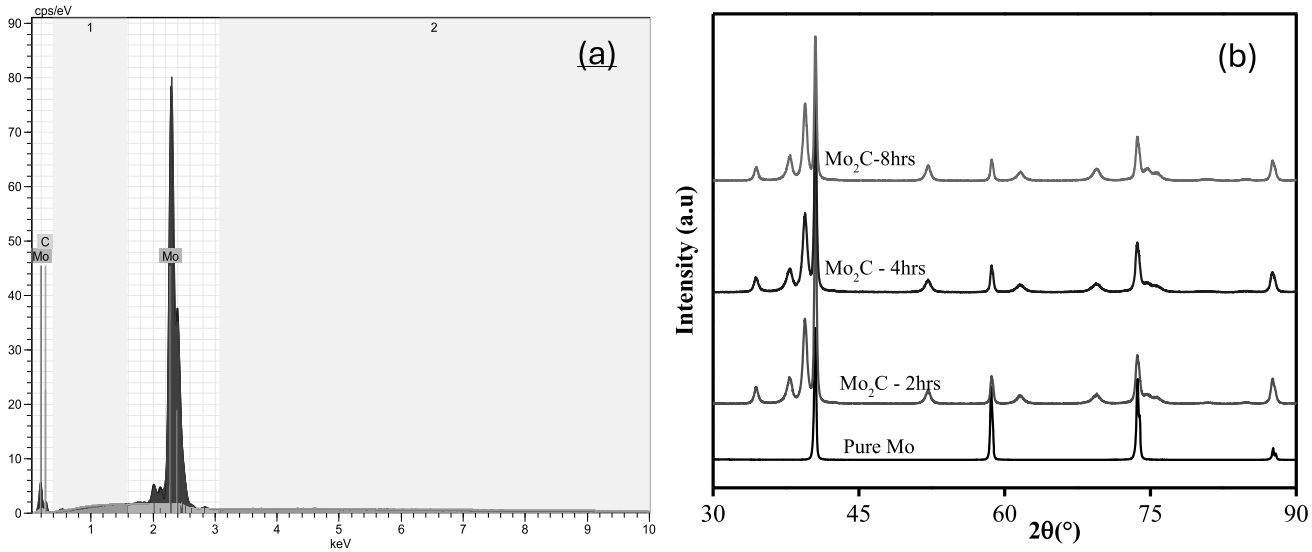

Fig. 2 **a** SEM–EDX and (**b**) XRD spectrums showing the presence of diffused carbon in the Mo discs

well with a standard XRD spectrum for Mo_2C obtained from ICSD, FIZ Karlsruhe, and represented reflections in the (100), (002), (101), (102), and (110) planes. The carbide layer was characterized as $\beta\ Mo_2C$ with a hexagonal close packed (hcp) crystal structure with the space group as $P6_3/mmc(194)$ [21].

3.3 Concentration profiles of carbon (3-mm Mo and Ti-Mo alloy)

Figure 3 presents the concentration profiles obtained from EPMA measurements on both electrode sides of the SPS-processed samples. For the 3-mm Mo discs annealed at 1000 °C, the upper electrode side showed a maximum carbon concentration of 20 at.%, which sharply decreased to 14.8 at.% within 40 µm before stabilizing at ~ 10.5 at.% beyond 300 µm. The lower electrode side exhibited different behavior: samples annealed for 1–4 h displayed an initial 17.5 at.% concentration that rapidly decreased to 14 at.% within 30 µm and then gradually declined to 11.5 at.% over 280 µm. Notably, the 8-h annealed sample showed higher carbon retention (maximum 17.5 at.%, minimum 13 at.%) over a shorter diffusion distance (230 µm). In the Ti-Mo alloy sample annealed at 1200 °C, the concentration of

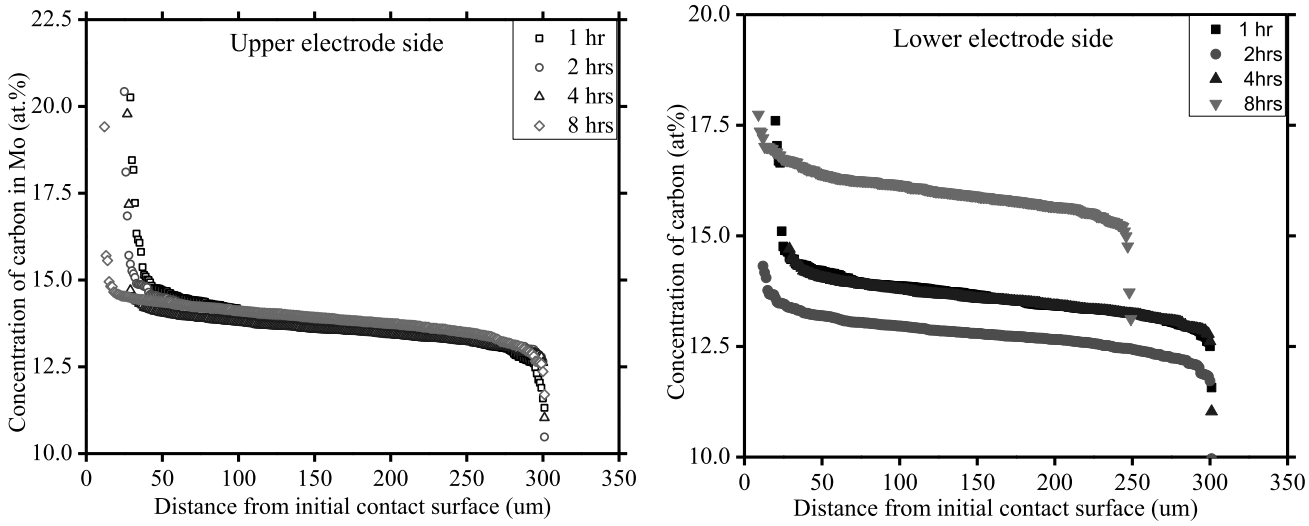

Fig. 3 Concentration profiles of carbon on the upper and lower electrode side of the 3-mm Mo discs annealed at 1000 °C for 1 h, 2 h, 4 h, and 8 h

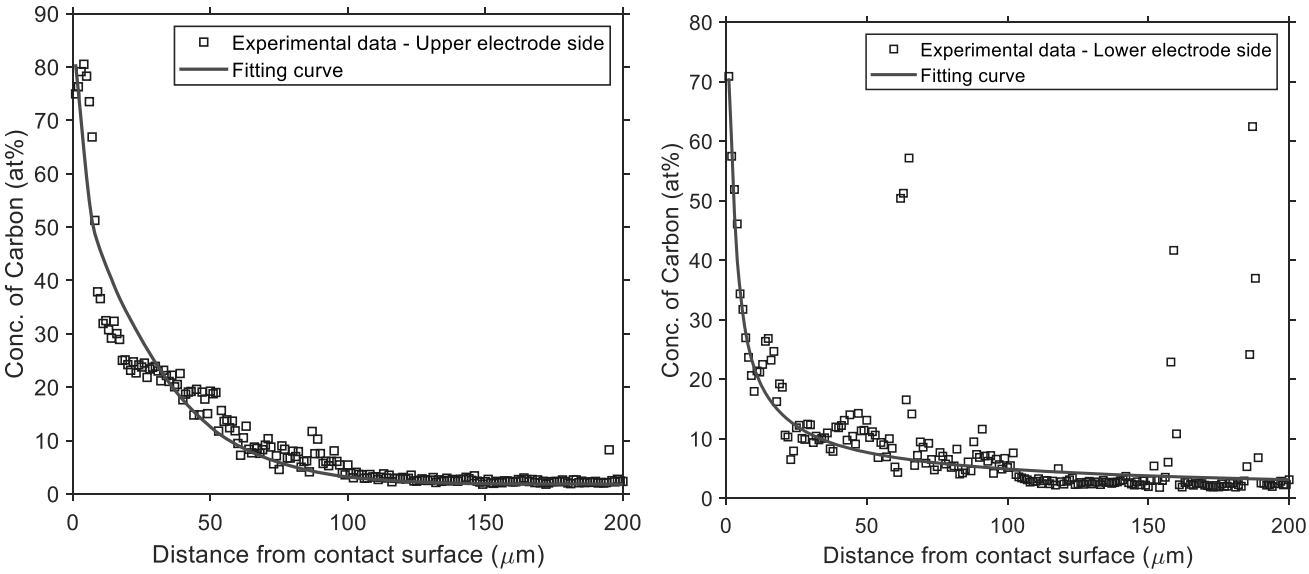

Fig. 4 Concentration profiles of carbon in Mo on the upper and lower electrode side of the Ti-Mo alloy sample

carbon in the Mo discs exhibited clear exponential decays: from 80.2 to 0.46 at.% (upper electrode) and from 70 to 1.61 at.% (lower electrode) across 200 μm (Fig. 4). In light of the fact that, in both cases (3-mm Mo and the Ti-Mo alloy samples), carbon diffused mainly in Mo discs, the concentration profiles showed strong temperature-dependent behavior with significant carbon penetration at elevated temperatures. Most importantly, the sharp decline in carbon concentration around 300 μm in the Mo disc (Fig. 3) and 200 μm in the Ti-Mo alloy (Fig. 4) suggests a mechanism that abruptly hinders carbon diffusion in Mo. This is likely due to the formation of a molybdenum carbide layer inhibits further carbon diffusion due to the structural differences between the carbide and pure Mo [9, 22]. Molybdenum has a body centered cubic (bcc) crystal structure which allows fast interstitial carbon diffusion while molybdenum carbide has a hexagonal close packed (hcp) crystal structure which introduces stronger Mo-C bonds and a less open lattice hence restricting carbon mobility and slowing down further carburization [23].

The carbon–sulfur analyzer measurements detected only trace amounts of carbon within the Ti-Mo interdiffusion zone (Table 1). Although Table 1 suggest minor carbon presence, the certified reference material (CRM) calibration tolerance (±0.004 wt%) on the carbon–sulfur analyzer for the Ti-Mo system renders these values statistically insignificant. This conclusion is further supported by the concentrations of carbon across the interdiffusion zone (edge vs. center) falling within instrumental error margins.

3.4 Microstructure of Mo_2C layer

Figure 5 are SEM-BSE micrographs showing the Mo_2C layer formed on the surface of the 3-mm Mo discs and on the Ti-Mo alloy sample. In the 3-mm Mo discs, the thickness of the Mo_2C layer ranged between 1.17 *and* 3.1 μm for the respective annealing time of between 1 and 8 h. From Table 2, it was observed that the thickness of Mo_2C layer increased with an increase in annealing time from 1.17 μm for 1 h to 3.10 μm for 8 h. A plot of the layer thickness against annealing time (Fig. 6a) for the 3-mm Mo discs confirmed parabolic growth rate of the Mo_2C layer [24]. In the Ti-Mo alloy sample, the thickness of the Mo_2C layer reached 17.7 μm (Fig. 6b).

Table 1 Concentration of carbon within the Ti-Mo interdiffusion region

S/no	Conc. at the edge (at.%)	Conc. at the center (at.%)
1	0.007327	0.000916
2	0.002914	0.000999
3	0.006494	0.001082
4	0.002414	-
Average conc	0.004837	0.000999

3.5 Microstructure of the Ti-Mo interdiffusion zone

Electron backscatter diffraction (EBSD) analysis identified a complex multiphase microstructure within the interdiffusion region. The primary phase consisted of a body-centered cubic β-(Ti-Mo) solid solution (space group $Im\bar{3}m$), which exhibited a bimodal grain structure. Quantitative analysis of the concentration profile revealed two distinct β-phase grains: a Mo-rich variant (18–46 at.% Mo, ~ 50 μm wide) and a Mo-lean variant (8–18 at.% Mo, ~ 72 μm wide), as evident in Fig. 7.

Additionally, the microstructure contained transformation products resulting from rapid cooling: a hexagonal α′ martensite ($P6_3/mmc$) and an orthorhombic α″ martensite ($Cmcm$), consistent with previously reported quenching effects [25]. These martensitic phases predominantly coexisted in a twinned morphology, as shown in Fig. 7. However, the EBSD analysis could not index a transition region (marked X in Fig. 7) bordering both the β phase and martensitic domains. Subsequent transmission electron microscopy (TEM) investigation resolved this region as an omega (ω) phase, whose characteristic fine-scale structure and diffraction patterns eluded EBSD detection. The ω phase was oriented along $(0001)_\omega \| (011)_\beta$ with respect to the β phase, and it was found to be 0.39 nm, and that of the β phase was 0.23 nm. A similar orientation of the ω phase was reported in the literature by Xing and San [26].

3.6 Diffusion coefficients of carbon in Mo

Figure 8 presents the concentration-dependent diffusion coefficients of carbon in 3-mm Mo discs annealed at 1000 °C for durations of 1–8 h, comparing results from both electrode sides. The data reveal two important trends. Firstly, the diffusion coefficients exhibited an inverse relationship with carbon concentration, decreasing sharply (10^{-13} to 10^{-15}–10^{-16} m^2/s) across a narrow concentration range (≤ 4 at.% C). This trend was particularly evident in the 1-h annealed sample, where upper and lower electrode sides showed reductions of two and three orders of magnitude, respectively. The second trend has to do with temporal evolution, in that, longer annealing times systematically lowered diffusion coefficients at all carbon concentrations. For instance, values for the 1-h annealed sample consistently exceeded those of samples treated for 2–8 h. The upper electrode side displayed an approximately linear decrease in diffusivity with increasing carbon content.

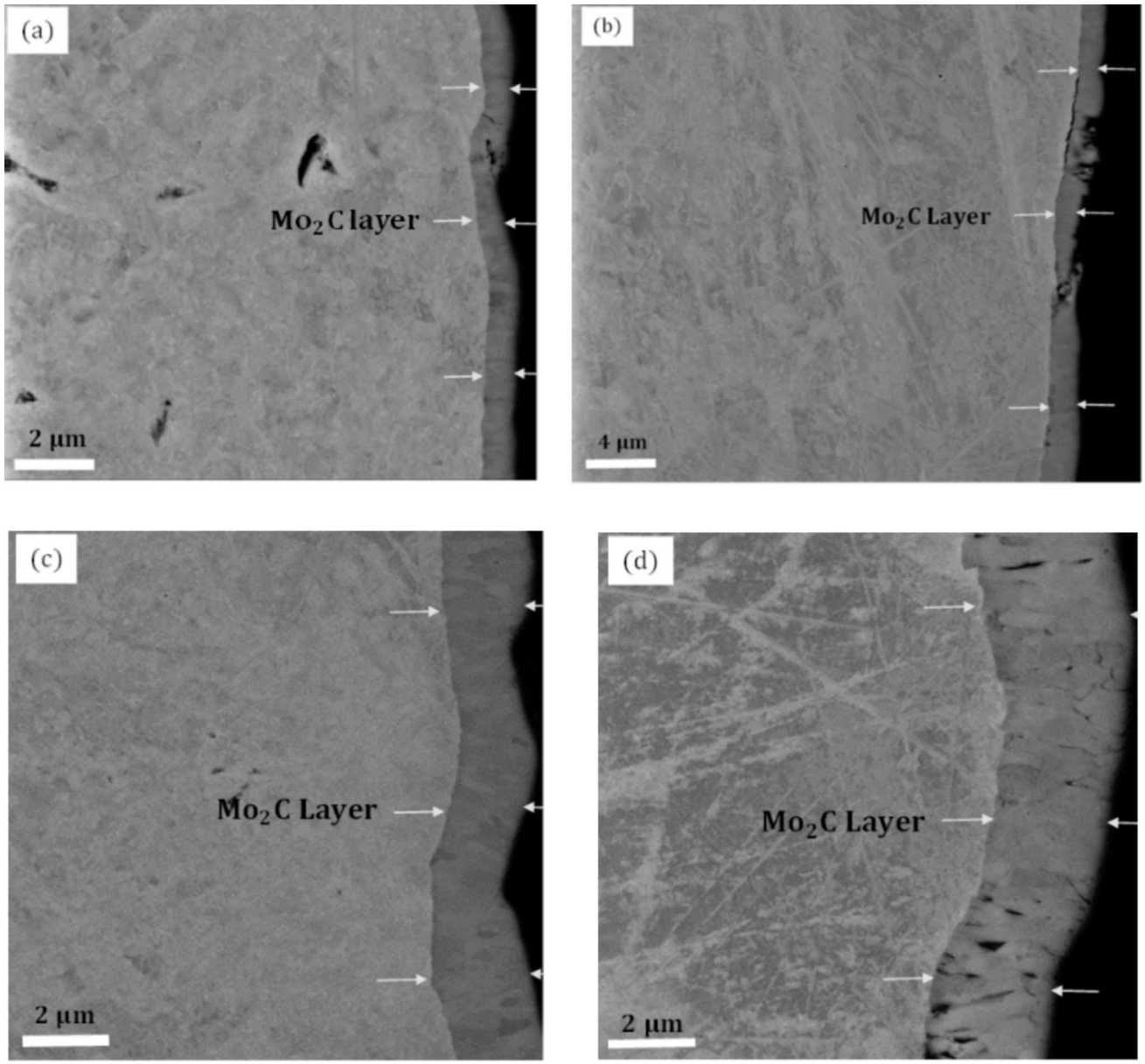

Fig. 5 Backscatter diffraction (BSD) images of Mo_2C layer in the sample annealed at 1000 °C for (**a**) 1 h, **b** 2 h, **c** 4 h, and (**d**) 8 h

Table 2 Molybdenum carbide layer thickness with annealing time

Sample	Temperature	Time (s)	Layer thickness (μm)
3-mm Mo discs	1000 °C	3600	1.17
	1000 °C	7200	1.85
	1000 °C	14,400	2.72
	1000 °C	28,800	3.14
Ti-Mo	1200 °C	14,400	17.7

These observations correlate with the formation of Mo_2C interfacial layers. The small atomic radius of carbon facilitates initial interstitial diffusion and grain boundary migration. However, as Mo_2C precipitates develop, they obstruct diffusion pathways—an effect amplified with prolonged annealing. This blocking mechanism explains the observed suppression of carbon mobility over time [27, 28], consistent with established models of interstitial diffusion in refractory metals.

The asymmetry in diffusion coefficients between the upper and lower electrodes likely stems from Joule heating variations during SPS annealing. Graphite foil exhibits higher electrical resistance than Mo [29–31], and its conductivity increases with temperature and pressure [32, 33].

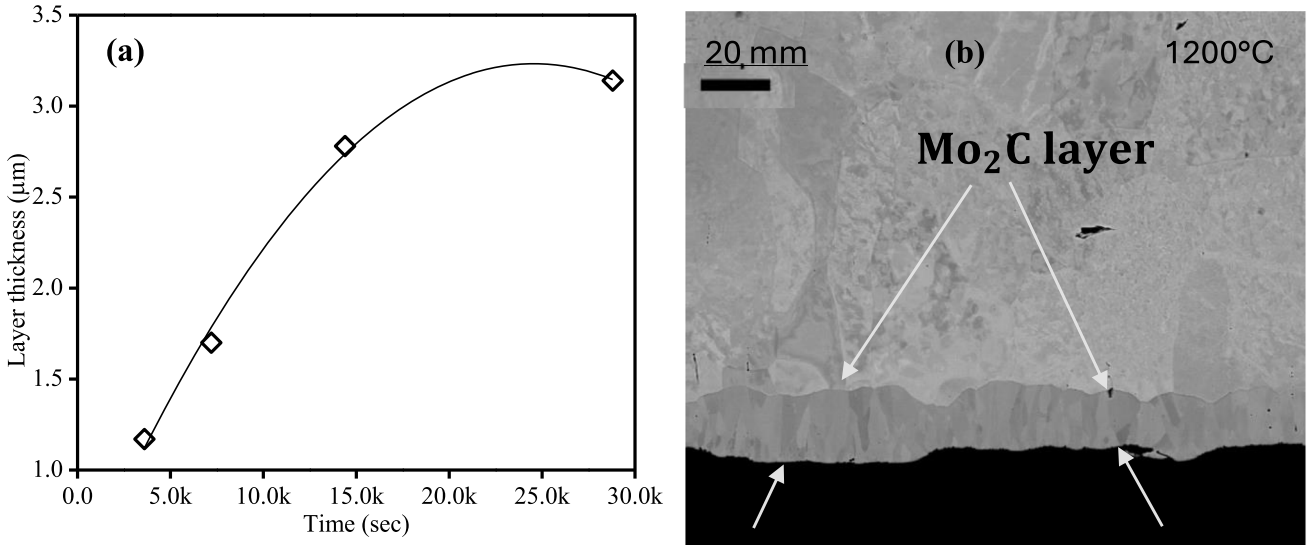

Fig. 6 **a** A plot of layer thickness against annealing time. **b** Backscatter diffraction (BSD) images of Mo_2C layer in the Ti-Mo alloy sample

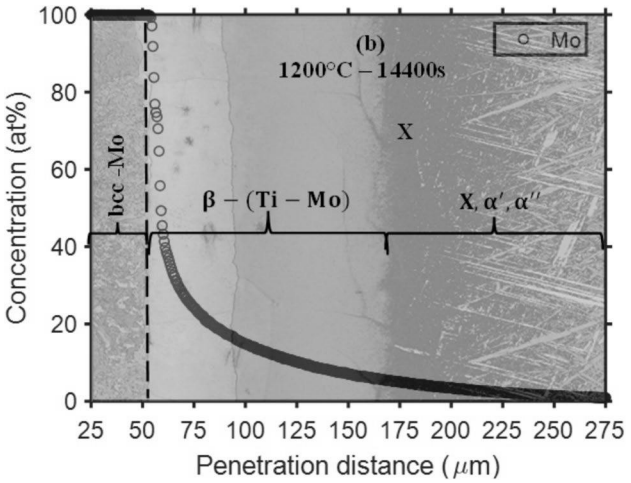

Fig. 7 Phase distribution across the interdiffusion region in the Ti-Mo alloy sample

Additionally, the formation of the resistive Mo carbide layer on either side of the Mo disc further alters the system's electrical properties as annealing progresses. Since heating in SPS relies on the Joule heating effect (resistive heating), these resistance differences across the C-Mo-C stack creates localized Joule heating disparities as well as thermal gradients hence influencing the diffusivity of carbon in Mo.

The Ti-Mo alloy sample (annealed at 1200 °C) exhibited strong concentration-dependent diffusion characteristics, as shown in Fig. 9. Quantitative analysis revealed on the upper electrode side; the diffusion coefficients decreased by two orders of magnitude (10^{-12} to 10^{-14} m^2/s) across a wide carbon concentration range (1.91–80.3 at.%). On the lower electrode side, a more pronounced reduction of the diffusion coefficients (10^{-13} to 10^{-16} m^2/s) occurred over a slightly narrower composition window (3.2–70.5 at.%). This systematic variation demonstrates that carbon diffusivity in the Ti-Mo system is highly sensitive to local carbon concentration. The asymmetric behavior between electrode sides may reflect differences in current density or thermal gradients during SPS processing.

3.7 Comparative analysis of diffusion coefficients

Possible enhancement of diffusion coefficients of carbon in molybdenum by the SPS process (in the presence of an electric current) was evaluated by comparing experimental interdiffusion coefficients with literature values, as shown in Fig. 10. Our results show that at lower carbon concentrations (< 14 at.%), excellent agreement exists between our measured values for 3-mm samples annealed at 1000 °C for 4 and 8 h, and those reported by Isobe et al. [24] and Imai et al. [28]. This consistency extends to the work of Isobe et al. [24] at 1200 °C, suggesting conventional diffusion behavior dominates in this concentration regime. However, marked deviations emerge at higher carbon concentrations. While literature values remain constant (Imai, Isobe, Shovensin et al. [34], Nishieda & Maclellan [35]), our data exhibit a clear inverse relationship between diffusivity and carbon content. Notably, Nishieda and Maclellan's 1000 °C data represent the upper extreme of reported values, exceeding

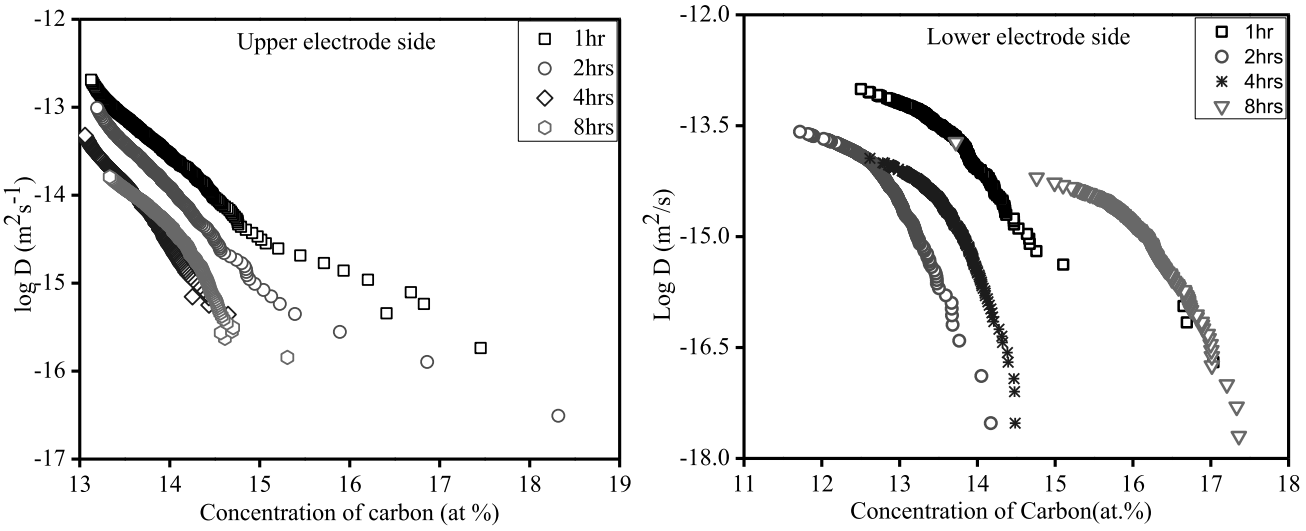

Fig. 8 Concentration-dependent diffusion coefficients of carbon on the upper and lower electrode side of the 3-mm Mo discs annealed at 1000 °C for 1 h, 2 h, 4 h, and 8 h

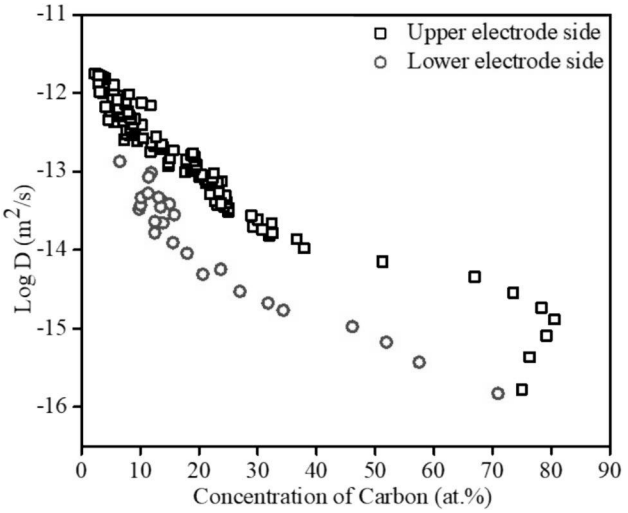

Fig. 9 Diffusion coefficients of carbon on the upper and lower electrode side of the Ti-Mo alloy sample annealed at 1200 °C for 4 h

our measurements by up to four orders of magnitude at 18 at.% C.

In the Ti-Mo alloy sample, the experimental diffusion coefficients agreed particularly with Isobe's and Kucera's results at low concentrations but diverges progressively above 10 at.% C. It must be noted however that in Kucera et al. [22], annealing was carried out at a much higher temperature of 1500 °C. Zhang et al. [9], using a method similar to this study but at 1500 °C, reported a diffusion coefficient of 10^{-11} m^2/s, matching Shovensin et al. [34] at 1100 °C and slightly exceeding Imai et al. [28]'s value of $10^{-11.4}$ m^2/s at 1200 °C. However, Zhang et al.'s [9] result was an order of magnitude lower than Shovensin et al.'s [34] $10^{-10.2}$ m^2/s at 1200 °C—despite the 300 °C lower temperature—raising doubts about diffusion enhancement during SPS annealing. Importantly therefore, no evidence of enhanced diffusion due to SPS processing was observed in this study as all measured values were within the range for conventional thermal diffusion in Mo-C systems. The results of the comparisons may also suggest that while carbon diffusion in molybdenum follows established behavior at dilute concentrations, significant deviations occur in carbon-rich regimes.

4 Conclusion

This investigation of carbon transport in molybdenum during spark plasma sintering (SPS) provides an insights into diffusion behavior under the tested conditions. At lower temperatures (below 1000 °C), the carbon concentration in Mo remained relatively constant, suggesting limited thermal activation of diffusion. At higher temperatures (1200 °C), carbon concentration in Mo increased close to fourfold, indicating thermally driven dissolution of carbon from the graphite foil into the Mo matrix. Both solubility and diffusivity of carbon appeared to become more concentration-dependent, in line with thermally activated interstitial diffusion mechanisms. The concentration profile exhibited a steep exponential gradient from the graphite foil/Mo interface to

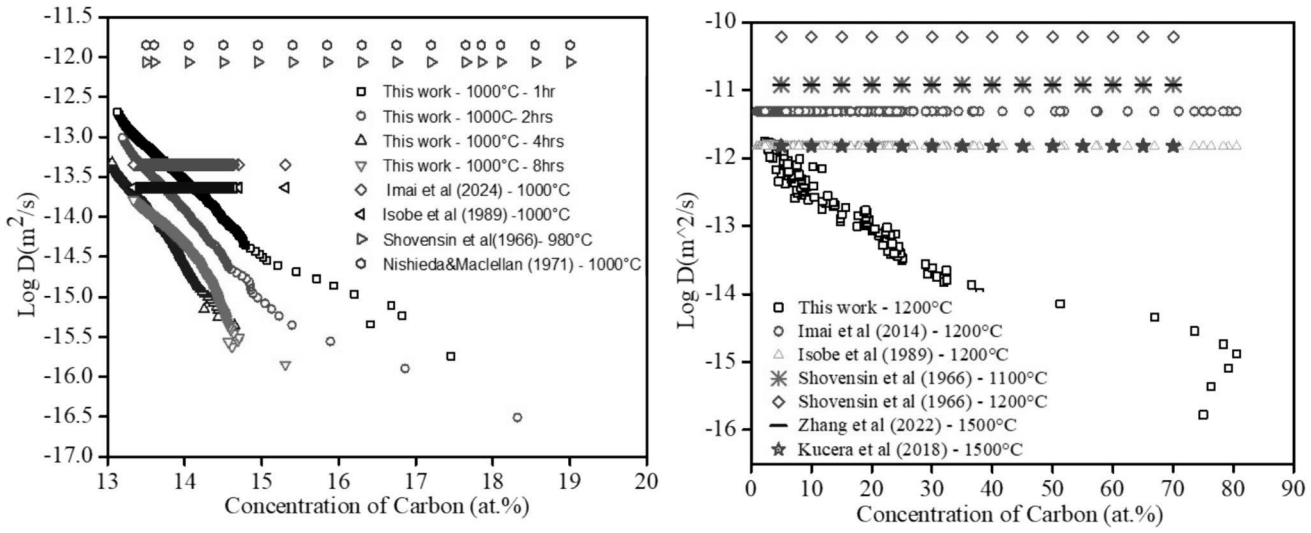

Fig. 10 Comparing the diffusion coefficients of carbon in Mo in the 3-mm Mo discs annealed

near-background levels over a short distance, consistent with rapid Mo-carbide formation inhibiting further carbon diffusion. While carbon penetration extended deeper into the Mo, it remained below the threshold for detectable carbide formation as revealed by the carbon–sulfur analyzer.

Under the specific experimental conditions applied in this study—vacuum annealing with 15 MPa uniaxial pressure, combined with alumina foil shielding to prevent carbon diffusion from die walls—no significant grain boundary-assisted carbon evaporation was detected. This contrasts with findings reported by Morita et al. [13, 36], highlighting the potential influence of processing parameters on carbon transport behavior.

The measured diffusion coefficients (10^{-15}–10^{-11} m^2/s) fell within the range expected for conventional thermal diffusion, and no clear evidence of SPS-specific enhancement of carbon mobility was observed under these conditions. This suggests that, for the parameters tested, electric current effects may have been secondary to thermal contributions. However, the absence of detectable enhancement does not preclude the possibility of such effects under alternative SPS conditions (e.g., higher currents, different pressure regimes, or modified die configurations). These findings contribute to the understanding of carbon transport kinetics in SPS-processed Mo while underscoring the need for further studies to explore the broader parameter space.

Acknowledgements We would like to acknowledge the support offered to us by Prof. David Rafaja, Dr. Salomon Anton, Dr. Mykhaylo Motylenko, and Ms. Diane Hübgen of the Institute of Materials Science at the TUBAF, Germany. One of the authors (WBM) would like to appreciate the support of the DUT Internal M and D Grants scheme and that of CEMEREM Kenya-Germany.

Author contribution All authors were fully involved at every stages of this work and they have read, edited, and approved the manuscript.

Funding Open access funding provided by Durban University of Technology.

Declarations

Competing interests The authors declare no competing interests.

References

1. Asoka-Kumar P, O'brien K, Lynn KG, Simpson PJ, Rodbell KP(1996) Detection of current-induced vacancies in thin aluminum–copper lines using positrons. Appl Physics Lett 68(3):406-408
2. Friedman JR, Garay JE, Anselmi-Tamburini U, Munir ZA (2024) Modified interfacial reactions in Ag–Zn multilayers under the influence of high DC currents. Intermetallics 12(6):589-597
3. Garay JE, Glade SC, Anselmi-Tamburini U, Asoka-Kumar P, Munir ZA (2004) Electric current enhanced defect mobility in Ni3Ti intermetallic. Appl Phys Lett 85(4):573–575

4. Hulbert DM, Anders A, Andersson J, Lavernia EJ, Mukherjee AK (2009) A discussion on the absence of plasma in spark plasma sintering. Scripta Materialia 60(10):835-838
5. Smetanina KE, Andreev PV, Nokhrin AV, Lantsev EA, Chuvildeev VN (2024) Carbon contamination during spark plasma sintering of powder materials: a brief overview. J Alloys Compd 973:172823
6. Sakajio M, Shter GE, Mann-Lahav M, Beilin V, Zamir S, Grader GS (2023) Carbon contamination prevention during spark plasma sintering. ACS Appl Mater Interfaces 15(31):38080-38089
7. Gild J, Floyd A, Sadowski B, Zhou T, Kim W, Bayya S, Sanghera J (2024) Temperature dependence of carbon contamination in spark plasma sintered Y2O3. J Eur Ceram Soc 44(6):4255–4259
8. Kim Y, Lee KH, Cha SI, Hong SH (2013) Effect of carbon contamination on microstructure and mechanical properties of SPS-consolidated molybdenum. J Alloys Compd 577:S588-S592
9. Zhang H, Li W, Chen X (2022) In-situ investigation of carbon diffusion in Mo during electric current-assisted sintering. Scripta Materialia 209:114380
10. Börner P, Kieback B (2017) Contamination control in SPS processing of refractory metals. In: Proceedings of the Euro PM2017 Congress & Exhibition. European Powder Metallurgy Association (EPMA)
11. Wang X, Zhang L, Fu Z, Wang H (2018) A review on contamination and its mitigation in spark plasma sintering. Crit Rev Solid State Mater Sci 43(6):493–512
12. Morita K, Kim BN, Yoshida H, Hiraga K, Sakka Y (2015) Spectroscopic study of the discoloration of transparent MgAl2O4 spinel fabricated by spark-plasma-sintering (SPS) processing. Acta Materialia 84:9–19
13. Morita K, Kim BN, Yoshida H, Hiraga K, Sakka Y (2018) Distribution of carbon contamination in MgAl2O4 spinel occurring during spark-plasma-sintering (SPS) processing: I–effect of heating rate and post-annealing. J Eur Ceram Soc 38(6):2588–2595
14. Conrad H (2000) Effects of electric current on solid state phase transformations in metals. Mater Sci Eng A 287(2):227–37
15. Mehrer H (2007) Diffusion in solide: fundamentales, methods, materials, diffusion-controlled processus. Berlin, Heidelberg: Springer Berlin Heidelberg
16. Kailasam JCLSK, Glicksman ME (1999) Evaluation of the methods for calculating the concentration-dependent diffusivity in binary systems. Metall and Mater Trans A 30:2605–2610
17. Larsson H (2021) On the use of Boltzmann's transformation to solve diffusion problems. Calphad 73:102261
18. Haußmann L, Bresler J, Neumeier S, Pyczak F, Göken M (2024) Interdiffusion coefficients and strengthening effects of Nb, Ta, and Zr in the α2-Ti3Al phase. J Phase Equilibria Diffus 45(4):764–771
19. Zhang Y, Jiang G, Zhao J, Liang L (2025) Investigation on electromigration-induced failure and reservoir effect in AlCu interconnects. Micromachines 16(4):458
20. Fischer ER, Hansen BT, Nair V, Hoyt FH, Schwartz CL, Dorward DW (2024) Basic scanning electron microscopy (SEM). Curr Protoc 4(6):e1034
21. Morris MC, McMurdie HF, Evans EH, Paretzkin B, Parker HS, Wong-Ng W, Gladhill DM (1979) Standard X-ray diffraction powder patterns: section 16--data for 86 substances. International centre for diffraction data: Department of Commerce, National Bureau of Standards, 1601, Park Lane Swarthmore, PA 19081
22. Kucera J, Million B, Čížek J (2018) Carbon diffusion in molybdenum: temperature dependence and grain boundary effects. J Nucl Mater 511:373–381
23. Bian B, Söltzer L, Muralikrishna GM, Taheriniya S, Sen S, Kumar KH, Wilde G, Divinski SV (2024) Grain boundary diffusion in a compositionally complex alloy: interplay of segregation, precipitation and interface structures in a Ni–Cr–Mo alloy. Acta Materialia 269:119803
24. Isobe Y, Son P, Miyake M (1989) Carbide layer growth behavior in a molybdenum coating on graphite at elevated temperatures. J Less Common Metals 147(2):261–268
25. Rastogi A, Sarkar R, Neelakantan S (2023) Transitions among martensitic phases during continuous deformation in metastable β Ti-10V-2Fe-3Al alloy. J Alloys Compd 964:171320
26. Xing H, Sun J (2008) Mechanical twinning and omega transition by⟨ 111⟩{112} shear in a metastable β titanium alloy. Appl Phys Lett 93(3)
27. Aleksandrov LN, Shchelkonogov VY (1964) The diffusion of carbon into tungsten and molybdenum at low carbon concentrations. Soviet Powder Metall Metal Ceram 3(4):288–291
28. Imai JI, Taguchi O, Tiwari GP, Iijima Y (2014) Diffusion of carbon in niobium and molybdenum. Mater Trans 55(12):1786-1791
29. Kim H, Lee S, Park J (2021) Thickness-dependent electrical resistivity of molybdenum thin films for interconnect applications. Mater Res Bull 133:111049
30. Mwaro WB, Mphahlele MR, Walker M (2024) Evolution of electrical resistance of graphite foils during spark plasma sintering. Int J Adv Manuf Technol 133(11):5683–5689
31. Chawake N, Pinto LD, Srivastav AK, Akkiraju K, Murty BS, Kottada RS (2014) On Joule heating during spark plasma sintering of metal powder. Scripta Materialia 93:52–55
32. Park S, Lee J, Kim H, Choi W (2023) Pressure-induced reduction of electrical resistance in compressed graphite foil for high-pressure sensor applications. ACS Appl Mater Interfaces 15(12):15842–15851
33. Zhang Y, Wang L, Chen X (2023) Anomalous electrical transport in thermally annealed graphite foils: role of defect scattering and carrier mobility. Carbon 201:1098–1107
34. Shovensin AV, Shcherbedinskii GV, Minkevich AN (1966) Some characteristics of the diffusion of carbon in molybdenum carbide. Soviet Powder Metall Metal Ceram 5:880–884
35. Nishida K, McLellan RB (1971) The diffusivity of carbon in molybdenum. J Less Common Metals 2(2):173–178
36. Morita K, Kim BN, Yoshida H, Hiraga K, Sakka Y (2015) Assessment of carbon contamination in MgAl2O4 spinel during spark-plasma-sintering (SPS) processing. J Ceram Soc Jpn 123(1442):983–988